PROCEEDINGS OF SPIE

SPIEDigitalLibrary.org/conference-proceedings-of-spie

Tunable Fabry-Pérot interferometer integrated in a silicon waveguide of an on-chip optical platform for long infrared wavelengths

Julia Wecker, Karla Hiller, Toni Großmann, Susann Hahn, Steffen Kurth, et al.

Julia Wecker, Karla Hiller, Toni Großmann, Susann Hahn, Steffen Kurth, Christian Helke, Matthias Küchler, Danny Reuter, Jörg Martin, Alexander Weiß, Harald Kuhn, "Tunable Fabry-Pérot interferometer integrated in a silicon waveguide of an on-chip optical platform for long infrared wavelengths," Proc. SPIE 12426, Silicon Photonics XVIII, 124260M (13 March 2023); doi: 10.1117/12.2650524

SPIE.

Event: SPIE OPTO, 2023, San Francisco, California, United States

Downloaded From: https://www.spiedigitallibrary.org/conference-proceedings-of-spie on 14 Nov 2023 Terms of Use: https://www.spiedigitallibrary.org/terms-of-use

Tunable Fabry-Pérot Interferometer integrated in a silicon waveguide of an on-chip optical platform for long infrared wavelengths

Julia Wecker*[a, b], Karla Hiller [a, b], Toni Großmann [a, b], Susann Hahn [b], Steffen Kurth [a], Christian Helke [a, b], Matthias Küchler [a], Danny Reuter [a, b], Jörg Martin [a], Alexander Weiß [a, b], Harald Kuhn [a, b]
[a]Fraunhofer ENAS, Technologie-Campus 3, 09126 Chemnitz, Germany; [b]Technische Universität Chemnitz, Center for Microtechnologies, Reichenhainer Str. 70, 09126 Chemnitz, Germany

ABSTRACT

As part of a future optical platform on-chip, we present a waveguide integrated tunable Fabry-Pérot Interferometer (FPI) for the long infrared wavelength range. The FPI consists of two parallel Bragg reflectors that are located at the ends of two waveguides facing each other. The waveguides are made of silicon and are suspended in air. The reflectors are realized as an alternating stack of silicon and air layers with high (H) and low (L) refractive index. The filter transmittance is evaluated by analytic calculations and electromagnetic finite difference time domain simulations. Filters with $(HL)^2$ layer stack show a full width half maximum of 270 nm and a peak transmittance of more than 25% at a wavelength of 9.4 µm at the first interference order in the simulation. It is evaluated by measurements.

A MEMS actuator is used to tune the filter wavelength by changing the distance between both reflectors. A digital electrostatic actuator concept with a linear drive characteristic, designed for a large travel range up to 4 µm with a driving voltage of less than 30 V, is presented and evaluated together with the filter.

The MEMS fabrication process for the structures is based on bonding and deep reactive ion etching (DRIE). The DRIE etch process was optimized, hereafter achieving a reduced roughness of less than 3 nm of the waveguide sidewalls.

For transmission measurements the silicon waveguides are coupled to a laser source and a detector using optical fibers together with optical couplers on the chip. The filter performance was characterized in the range from 9µm to 9.4 µm.

Keywords: Fabry-Pérot-Interferometer, tunable filter, optical waveguide, silicon photonics, infrared, MOEMS, photonic integrated circuit (PIC)

1. INTRODUCTION

The development of very small size and low-cost spectrometers for the infrared wavelength range that are suitable for a great variety of use cases is in the focus of many publications [1-4]. Modular approaches with the integration of components like waveguides, bends and couplers on one single chip are reported [5, 6]. The evanescent field of waveguides in the mid and long infrared wavelength range is used for spectral analyses of gases [7-9]. In general, spectrometers can be distinguished according to their wavelength selecting principle in grating based diffraction spectrometers (e.g. supplied by Hamamatsu), Hadamard transform spectrometers, MEMS-based Fourier transform spectrometers, Fabry-Pérot interferometer (FPI) based spectrometers, and spectrometers with linear optical filters and multi spectral sensors. In the development towards single chip spectrometers mainly MEMS-based Fourier transform spectrometers are on focus [2, 10, 11, 12] followed by in-plane FPIs [13]. Such FPI filters are of particular interest because of their high integration potential.

In-plane FPIs were presented by several research groups in the last years. Most of them are designed for 1.5µm wavelength, like Sabry [13], Lin [18] or Omran [19]. Goh [20] presents an in-plane FPI for 3.3 µm to 4.5 µm wavelength. The wavelength range around 9 µm was not addressed so far. As all these publications use vertical Si/Air Bragg reflector configurations in combination with fixed and tunable cavities (with Si thickness ranging from 5 µm up to 80 µm), the accuracy of the Si etch process plays an important role. Main issues for an in-plane FPI are the deviation of pattern width from the design values due to mask undercut, the verticality and the sidewall roughness of the distributed Bragg reflector layers. The sidewall roughness will strongly influence the optical finesse of the waveguides and filter due to scattering losses. As an example, Goh [20] achieved a sidewall roughness of 12 nm (measured on an area of 15 µm x 15 µm) for 1.2 µm air space and 1.25 µm silicon layer width, using a typical DRIE multiplex etch process.

*julia.wecker@enas.frauhofer.de; phone +49 371 45001 613; enas.fraunhofer.de

Silicon Photonics XVIII, edited by Graham T. Reed, Andrew P. Knights,
Proc. of SPIE Vol. 12426, 124260M · © 2023 SPIE
0277-786X · doi: 10.1117/12.2650524

Downloaded From: https://www.spiedigitallibrary.org/conference-proceedings-of-spie on 14 Nov 2023
Terms of Use: https://www.spiedigitallibrary.org/terms-of-use

The targets of this work will contribute to further improvement of the design and of the fabrication technology for electrically tunable wavelength filters as part of an integrated spectroscopic system or even as functional component of a photonic integrated circuit (PIC) for applications in the mid infrared wavelength range up to 12 µm wavelength. The development goals for such kind of electrically tunable wavelength filters are

- High passband transmittance
- Sufficiently high wavelength selectivity and wavelength tuning range
- Digital control of the filter wavelength
- Small outline
- Affordable cost and low complexity of the fabrication technology

In this paper we present an in-plane tunable FPI for 8 µm to 10 µm wavelength range for the application of gas measurement, hereby especially addressing the ethanol absorption at 9.4 µm. While the in-plane FPI described in the state of the art are mainly coupled to fibers or plane waves in free space, we present an FPI which is directly integrated in a multi-mode silicon waveguide [22] with 15 µm height. The Si/Air distributed Bragg reflectors (DBR) are attached to the waveguide ends.

In order to achieve a high over all transmission, one need to consider the coupling with other functional sub-components beside of the FPI (within the PIC or to external components) and in addition the absorption loss in the FPI. It is necessary to optimize the transmission of the waveguides due to evanescent field and due to extinction in the waveguide material. Because of the limited aperture of the FPI, further loss by stray fields is expected and needs to be considered. Moreover, detrimental effects reducing the transmittance are discussed based on analytical and numerical analysis of the FPI configuration in this paper. The optical characteristic of the FPI is evaluated by analytic calculations and electromagnetic finite difference time domain simulations (FDTD) with CST Microwave Studio®.

The wavelength selectivity is mainly influenced by the reflectance of the FPI reflectors and by their roughness, waviness and by their parallelism and wavefront shape. The presented work describes how an optimized etching technology leads to reduced roughness and waviness of the reflectors.

The FP cavity can be tuned by an electrostatic MEMS actuator. Most of the electrically tunable FPI shown in the literature are controlled by an electrostatic actuator by analogously variation of the applied voltage with its inherent quadratic dependency of the electrostatic force and deflection on the applied voltage. Even when the filter is tuned to maximum deflection, a small variation of the voltage leads to strong changes of the tuning state and of the passband wavelength. It leads to a potentially higher error sensitivity and bears the risk of electrostatic pull-in. This paper shows how a digitally operated electrostatic MEMS actuator is used for tuning of a FPI that does not have such undesired effects.

The filters were tested for scanning the spectrum of a quantum cascade laser (QCL) with a spectral band from 9.0 µm to 9.4 µm (QF9150C2, Thorlabs).

2. FPI THEORY

The Airy function describes the transmittance of an ideal FPI [15]:

$$T(\lambda) = T_{pk}\left[1 + \frac{4R}{(1-R)^2}\sin^2\left(\frac{2\pi n d\cos\theta}{\lambda} - \Phi(\lambda)\right)\right]^{-1} \tag{1}$$

with R the reflectance, Φ the phase dispersion of the reflectors and d the distance between the reflectors. T_{pk} is the peak transmittance calculated from the reflectance and the absorbance A.

$$T_{pk} = \left(1 - \frac{A}{1-R}\right)^2 \tag{2}$$

The wavelength resolution is given by the full width at half maximum FWHM [16]:

$$FWHM = \frac{\lambda(1-R)}{m\pi\sqrt{R}} \tag{3}$$

The reflectance R of the FPI reflector as a stack of alternating quarter wavelength thick layers of high and low reflective index is calculated for a given wavelength, in case that the medium between the reflectors is the same as the low reflectance layer and the substrate medium of the reflector is similar to the high reflectance layer [17]:

Downloaded From: https://www.spiedigitallibrary.org/conference-proceedings-of-spie on 14 Nov 2023
Terms of Use: https://www.spiedigitallibrary.org/terms-of-use

$$R = \frac{1-\left(\frac{n_H}{n_L}\right)^{2p}\left(\frac{n_L}{n_H}\right)}{1+\left(\frac{n_H}{n_L}\right)^{2p}\left(\frac{n_L}{n_H}\right)} \quad (4)$$

With n_H and n_L the refractive index of the high reflectance layer and the low reflectance layer and p the number of alternating layer pairs. The reflectance increases with the number of layer pairs. Equation 4 is only valid for the central wavelength of the reflector where the layer thickness is equal to quarter wavelength. It was used here for estimating the numbers of reflectors necessary for achieving a proper reflectance. For evaluation of the spectral reflectance the transfer matrix method or FDTD simulation software can be used. This gives additional information like the bandwidth for that the reflectance reaches a specified value.

3. DESIGN

The integrated in-plane platform consists of the edge and grating couplers, waveguides, distributed Bragg reflectors and the FP cavity forming the filter, which is coupled to an electrostatic actuator for tuning the cavity and hence the transmission wavelength. While the grating couplers and waveguides have been investigated before (see [22]), we focus on the components and the combination of the tunable filter.

3.1 Waveguide with distributed Bragg reflector

The DBRs are designed as $(HL)^2$ stacks of silicon (H) and air (L) with the waveguide being the first H-layer (see Figure 2a). The L-layer has a thickness of ¼ wavelength at 9.4 µm, which is 2.35 µm. For compatibility with design rules from MEMS foundry service such as XMB 10 from X-FAB, where the smallest lateral dimension is 2 µm, the H-layer thickness was chosen to be ¾ wavelength. With the refractive index of n=3.42 of Si at a wavelength of 9.4 µm, this results in a layer thickness of 2.06 µm.

Calculated with equation 4 the reflectance R at 9.4µm is 90% for the $(HL)^2$ stack. Due to the ¾ wavelength H-layer the bandwidth is reduced compared to a ¼ H-layer. But the bandwidth is still sufficient for the addressed wavelength range.

Reflectance and absorptance of the reflector at the waveguide end with cross section of 15 µm by 30 µm were simulated in the wavelength range 8.8 µm to 9.6 µm by electromagnetic FDTD simulation with CST Microwave Studio®. The absorptance of the reflector mainly influences the peak transmittance of the FPI. It depends on the extinction coefficient of the reflector materials. The extinction coefficient k of silicon shows a strong peak around 9 µm [21] caused by oxygen absorption. It increases for highly conductive silicon. For the simulations and calculations, that were performed to design the FPI, refractive index and extinction coefficient from silicon with resistivity of 3 kΩcm was used. The extinction coefficient is plotted in Figure 1 for 8 µm to 10 µm wavelength range.

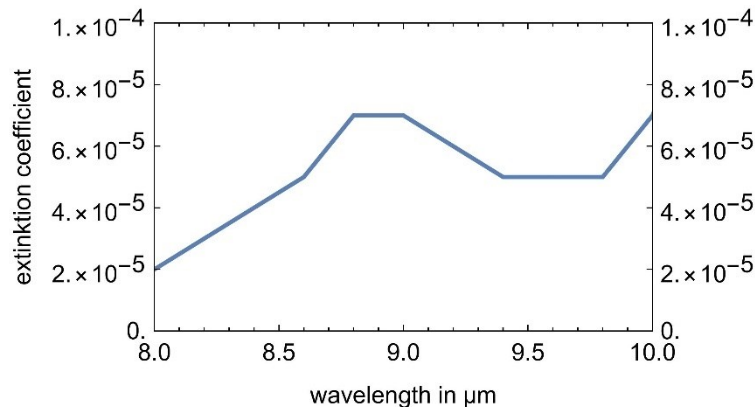

Figure 1. Extinction coefficient of silicon with resistivity of 3 kΩcm.

Figure 2 shows a model of a section of the end of e rectangular waveguide including a DBR and a waveguide port (Fig. 2a), the resulting electric field distribution (Fig. 2b) as well as the simulation results of the absorption and reflection (Fig. 2c). Compared to the calculation applying equation 4, which is based on the assumption of infinitely large reflectors, the simulation takes into account the small lateral dimension of the reflectors as well as diffraction effects and stray fields that can be seen from the electric field distribution in Figure 2b. The reflectance is 84% at 9.0 µm and 87% at 9.4 µm

Downloaded From: https://www.spiedigitallibrary.org/conference-proceedings-of-spie on 14 Nov 2023
Terms of Use: https://www.spiedigitallibrary.org/terms-of-use

wavelength. It is only slightly reduced compared to the calculation with equation 4. The absorption is 7% at 9.0 µm and 6% at 9.4 µm wavelength.

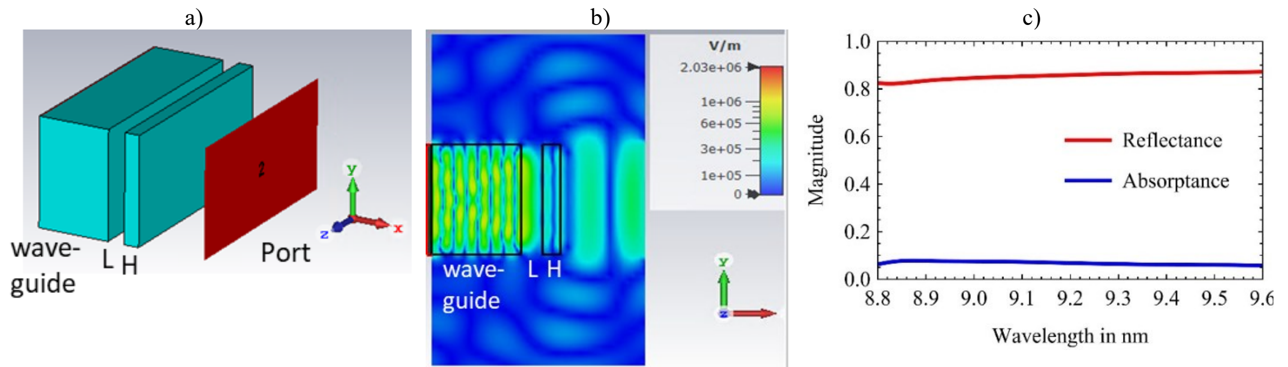

Figure 2. Bragg reflector at waveguide end (H-LH-L) simulated in CST Microwave Studio® a) Simulation model, b) electric field c) reflectance and absorptance of the Bragg reflectors in the band of interest.

3.2 Fabry-Pérot Interferometer

To form the FPI two waveguides with Bragg reflector ends are facing each other (see Figure 3a). The transmittance of the FPI was simulated for different reflector distances. A reflector distance of 4.9 µm results in a central wavelength of 9.44 µm (1st order filter configuration). This is lower than twice the reflector distance due to a significant phase distortion of the reflector. The FWHM for a central wavelength of 9.44 µm of the FPI is approximately 270 nm. The peak transmittance is > 25%. In contrast to the analytical calculation (section 2), the simulation shows a lower peak transmittance, because in the analytical calculation an infinitely extended reflector is considered and diffraction effects and stray fields are neglected. The influence of the high extinction value of silicon around 9 µm wavelength causes a dip in the left side of the transmittance peak for d < 4.7 µm. It is assumed that the FWHM would be slightly broader without this influence.

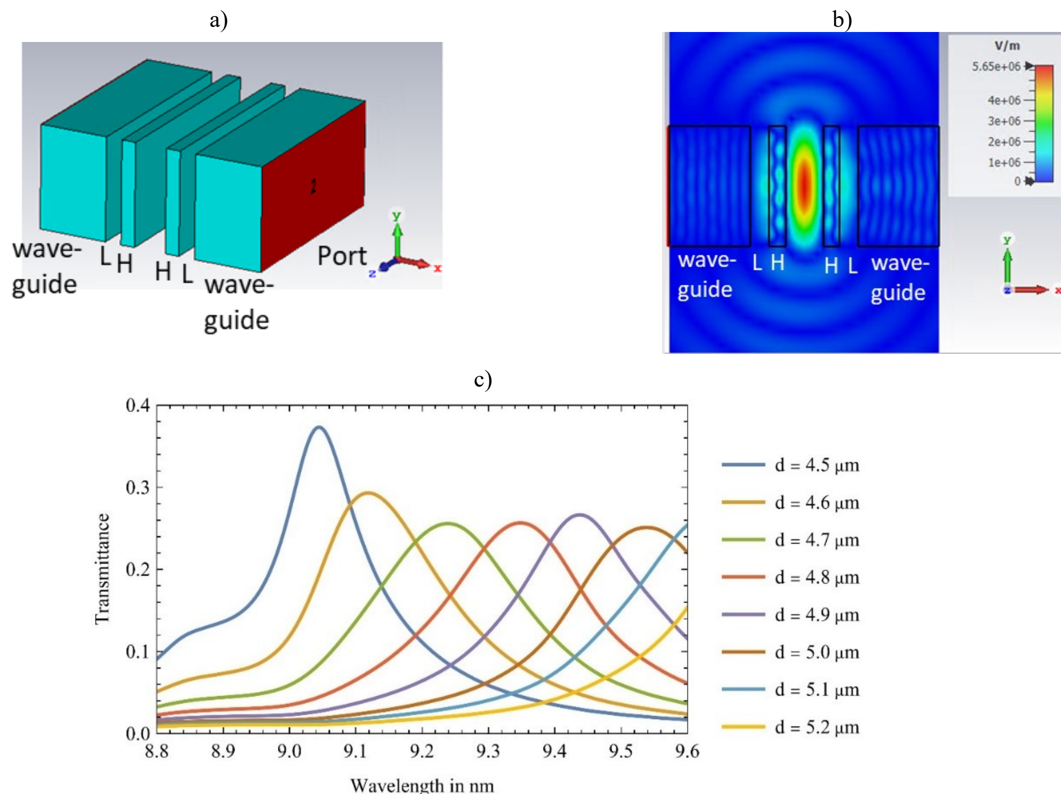

Figure 3. Simulated in CST Microwave Studio® a) Simulation model and b) electromagnetic field at peak transmittance, c) Transmittance of first order FPI for different resonator distances d between the reflectors.

Downloaded From: https://www.spiedigitallibrary.org/conference-proceedings-of-spie on 14 Nov 2023
Terms of Use: https://www.spiedigitallibrary.org/terms-of-use

3.3 Wavelength tuning

Figure 4 shows the concept of the tunable FPI integrated in the optical platform. The light is coupled into the tapered waveguide via a grating coupler, passes the FP filter and the transmitted light is coupled to the detector with an edge coupler based on an optical fiber.

The wavelength of the FPI is tuned by increasing the distance between the reflectors (see Figure 3c). Therefor one of the reflectors is mechanically connected to an electrostatic MEMS actuator with comb structures. It allows to increase the distance by a maximum of 4 µm in addition to the 3.2 µm initial gap. The distance change is digitally resolved via 8 actuator stages (A1…A8 shown in Figure 5), each with half the travel range of the previous stage. Similar actuators have been presented by Sarajlic [23] and Pitchai [24]. The size of the actuator surface, or the number of effective comb structures, determines the force exerted on the springs. The resulting deflection depends on the stiffness of the springs holding the push rod. The actuator was designed for a maximum deflection of 3 µm (tuning from 3.2 µm to 6.2µm) at a control voltage of 27 V. The spring stiffness per spring is 30 N/m. The size of the actuator area and thus the deflection of an actuator stage at the same drive voltage are reduced by half from A1 to A8 in each case. Thus, a resolution of 8 bits for the full travel range is realized. This corresponds here to a deflection of 11.7nm for LSB the least significant bit and thus a resolution of the adjustable central wavelength of approximately 23 nm for the first interference order.

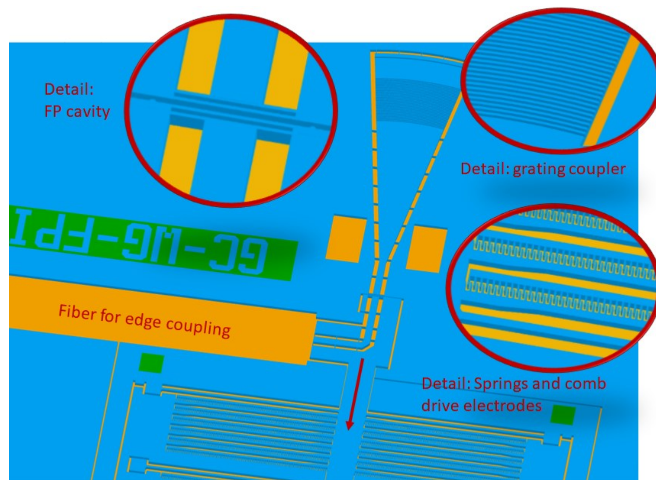

Figure 4. FPI embedded in the optical in-plane platform.

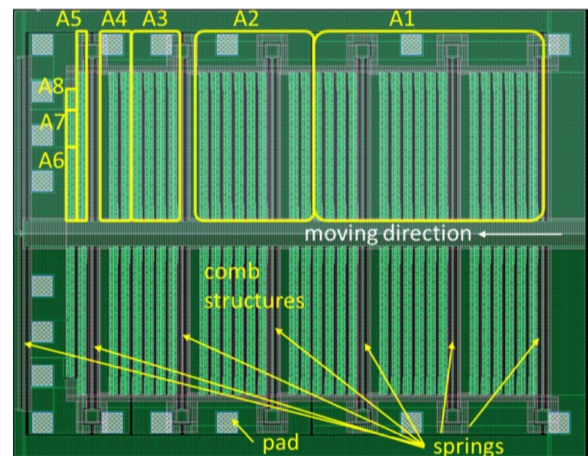

Figure 5. MEMS actuator design with 8 actuator stages.

4. MEMS FABRICATION TECHNOLOGY

Our design approach requires both electromechanical and (multimode) optical functionalities for MIR, which are built the same Si device layer, and furthermore support different types of couplers for in coupling and out coupling of the light. Furthermore, electrical contacts are needed for applying drive voltages to the electrostatic actuators. An appropriate technology approach based on a cavity-SOI technology has been chosen in order to provide all required functionalities. A schematic cross section is shown in Figure 6.

The technology flow has been adopted from our BRDIE technology flow [25] developed originally for inertial sensors. Several adjustments, compromises and improvements have been worked out in order to meet the specific requirements of the single elements, which are discussed in the following:

Firstly, for the doping level of the Si device layer exist contradictory requirements from the optical and electrical perspective: while it should be high to obtain good ohmic Al/Si contacts and low resistivity towards the electrodes, this would seriously disturb the optical functionality in NIR and MIR (high absorption losses). Therefore, Si with specific resistivity > 1 kΩcm has been chosen, hereby accepting in the first approach the non-ideal Al/Si contact. Further improvements can be obtained either by local doping in the contact and electrode areas or by covering the electrodes completely with Al (e.g. using selective sputtering via a shadow mask).

Downloaded From: https://www.spiedigitallibrary.org/conference-proceedings-of-spie on 14 Nov 2023
Terms of Use: https://www.spiedigitallibrary.org/terms-of-use

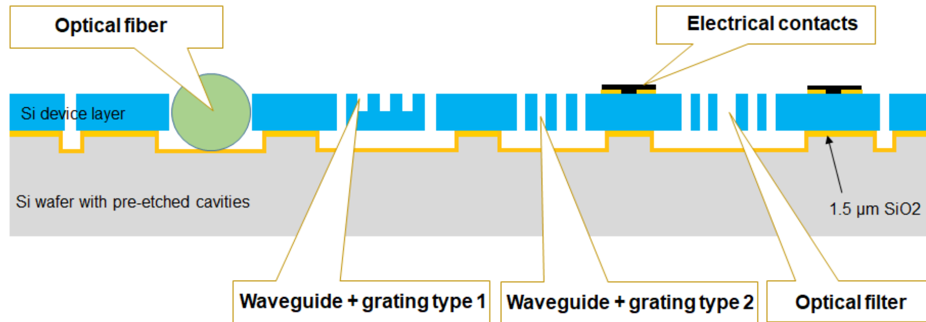

Figure 6. Schematic cross section of the cavity-SOI MOEMS (not to scale).

Secondly, the optical losses of the waveguides and filter (built by Si/air Bragg layer stacks) are strongly influenced by the surface and sidewall roughness of the Si structures. Usually, for patterning of the Si by DRIE etching, the so-called "Bosch" process is applied, which is based on alternating isotropic Si etch steps, surface passivation and anisotropic removal of the passivation on horizontal surfaces. This leads to the typical etch profile as shown in Figure 7a and b. For our "standard" precision Si etch process, we have measured a rms roughness of more than 5 nm (measured with a white light interferometer (Zygo) on an area of 10 µm x 40 µm). The rms roughness depends strongly on the width of the etched grooves. For small groove widths the roughness exceeds values of 60 nm rms.

Several methods are known for reducing this surface roughness, such as subsequent isotropic over etching or subsequent thermal oxidation followed by oxide etching. However, these methods suffer from changing the lateral dimensions of the patterns (widening the space between the structures); hence it would be difficult to obtain the small air gaps e.g. in the Bragg reflector regions. On the other hand, complete anisotropic (physical) etching comes along with a low selectivity, hence very thick mask layers are required for deep Si etching, or the etch depth is very limited.

As a compromise, our approach is based on a modified "Bosch" process [26], using a more anisotropic etch step, and a series of very short etch steps are combined (see Figure 7c, d). As a result of this improvement, the rms roughness of the waveguide sidewalls was measured a best value of 2 nm (measured with a white light interferometer (NewView 7300, Zygo) on an area of 10 µm x 40 µm, groove width at the waveguide side wall is 20 µm). Furthermore, as can be seen in Figure 7d, there is almost no mask undercut visible, although a certain critical dimension loss has been measured compared to the mask layout when applied in the full process flow (see Figure 11). In Figure 7e, the etch profile of 2 µm lines and 2 µm trenches test pattern, etched into the full material to 15 µm etch depth is shown. The etch profile is slightly negative tapered with a sidewall angle of approx. 90.1°.

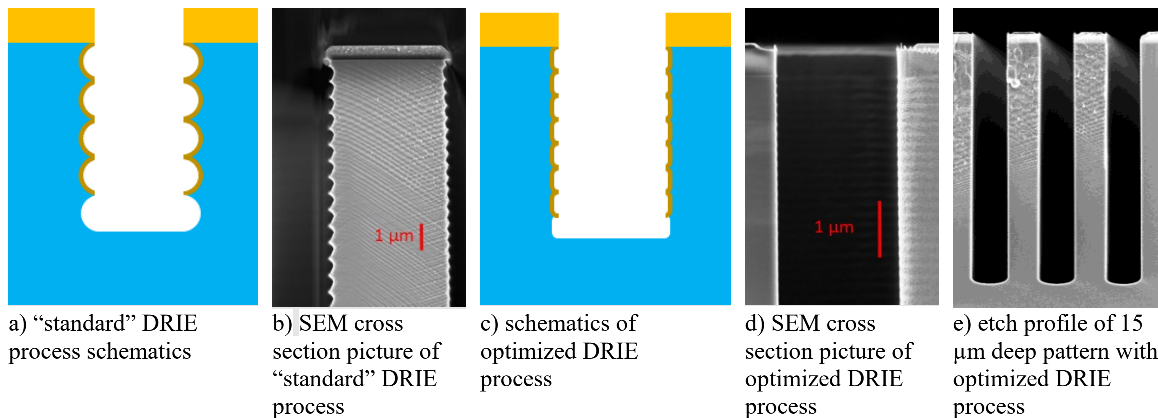

a) "standard" DRIE process schematics
b) SEM cross section picture of "standard" DRIE process
c) schematics of optimized DRIE process
d) SEM cross section picture of optimized DRIE process
e) etch profile of 15 µm deep pattern with optimized DRIE process

Figure 7: Comparison of "standard" Bosch process with > 5 nm rms roughness (a, b) with modified process for improved sidewall smoothness of 2 nm rms (c, d, e)

A third aspect is the appropriate choice of the Si thickness. From the optical point of view, very thin < 1.5 µm Si layers can provide single mode waveguides. However, from the mechanical and electrostatic point of view, a higher thickness is favored in order to provide a higher stability of the (mechanical) structures. On the other side, restrictions are given by the

Downloaded From: https://www.spiedigitallibrary.org/conference-proceedings-of-spie on 14 Nov 2023
Terms of Use: https://www.spiedigitallibrary.org/terms-of-use

selectivity and the achievable aspect ratio of the etch process. Considering all these aspects, we have chosen a thickness of 15 µm for a first fabrication run, which finally provides multi-mode waveguides and built-in filters.

Next, in order to create grating couplers of type 1 (see Figure 6), a two-step etch process has been applied, using both 400 nm SiO_2 and 1.7 µm photoresist as masking layers. Finally, in order to enable edge coupling as well, the depth of the pre-etched cavity has been adjusted, that the middle line of the optical fiber meets the middle line of the Si device layer.

Combining all these considerations, the technology flow shown in Figure 8 has been proposed and developed. It starts with a 400 µm Si substrate, in which a cavity is dry etched into Si (etch depth 150 µm). A thermal oxide (thickness 1.5 µm) is grown in order to provide an electrical isolation between the basic and device silicon (a). Next, an SOI Wafer with 15 µm thick device layer with a specified electrical resistance of > 1 kΩcm (FZ wafer material) is directly bonded to the basic wafer, and the handle wafer is removed by grinding and etching down to the buried oxide (b). This oxide is removed as well, and a new PECVD oxide mask of 400 nm thickness is deposited and patterned with contact openings. Sputtered and patterned Al serves as contact pads for electrostatic actuators and for labels (c). The subsequent patterning step of the oxide is required for the grating couplers of type 1 (d). All mechanical structures are defined within the following photoresist mask with 1.7 µm thickness and are transferred into the masking oxide as well (e). In order to achieve gratings of type 1, the deep Si etch process is divided in two steps. First, all structures except these gratings are etched to more than the half device layer thickness (f). Next, the resist mask is removed (g), and the second etch step (via oxide mask) will adjust the depth of these gratings to be 7.5 µm (half of the device layer thickness). It has to be ensured that hereby all other structures are released. Finally, the oxide mask layer is removed by dry etching (i).

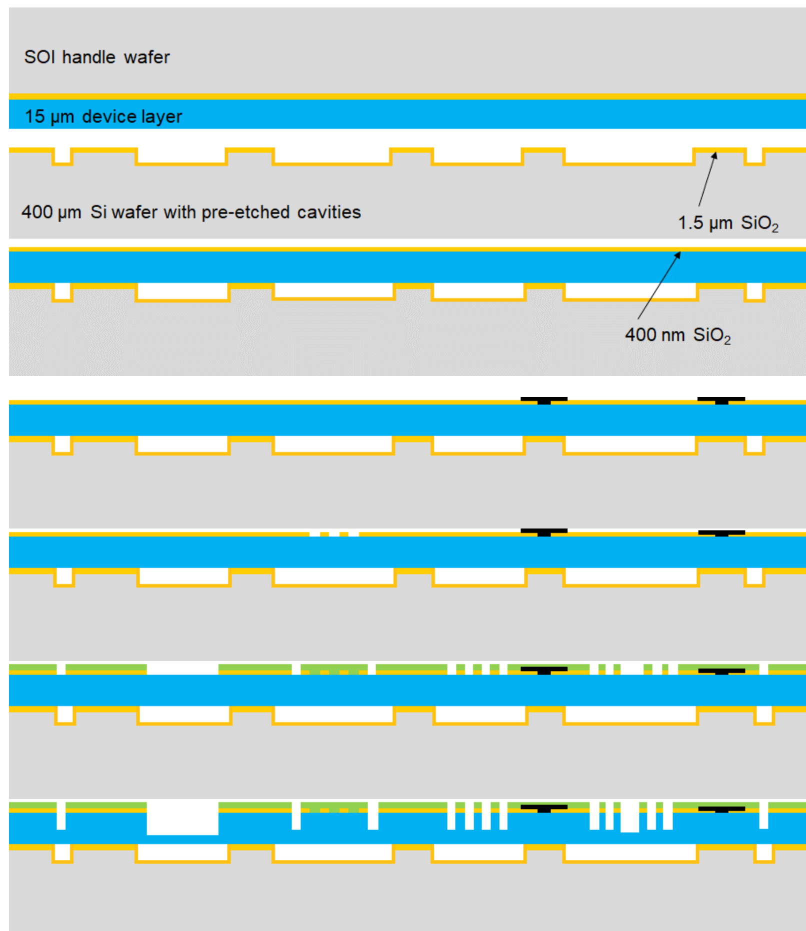

a) Etching of cavities into the Si basic wafer (etch depth adjusted for optical fiber thickness) and thermal oxidation. An SOI wafer with 15 µm device layer is provided as well

b) Direct bonding of the SOI wafer and handle wafer removal, removal of the bond oxide, deposition of new PECVD mask oxide

c) Etching of contact holes, Al deposition and patterning for electrical contacts

d) Patterning of oxide for gratings (stepper lithography)

e) Resist and oxide patterning (stepper lithography) for deep Si etch

f) Deep Si pre-etch with optimized DRIE process

Downloaded From: https://www.spiedigitallibrary.org/conference-proceedings-of-spie on 14 Nov 2023
Terms of Use: https://www.spiedigitallibrary.org/terms-of-use

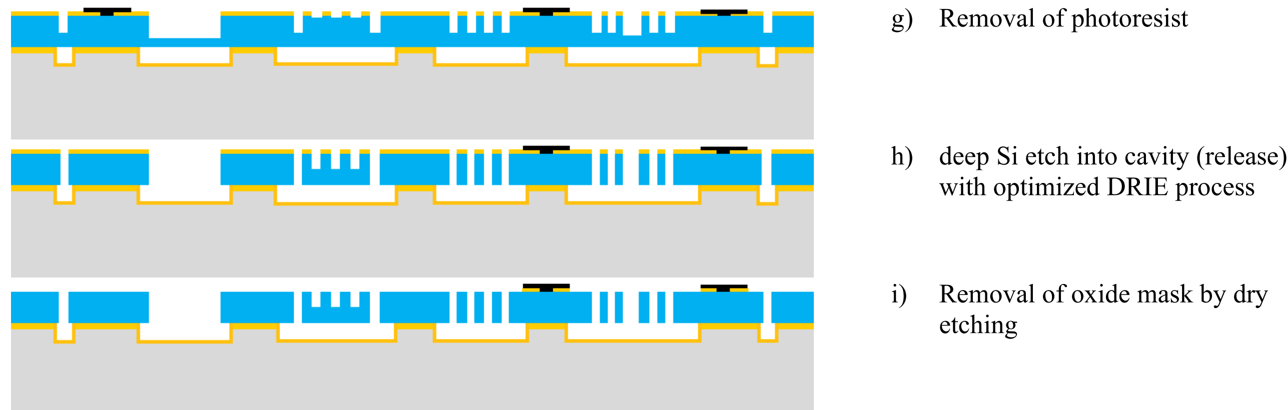

Figure 8. schematic process flow for the adopted cavity-SOI technology

The etch depth depends strongly on the mask opening width (well-known aspect ratio depending etching – ARDE effect). In order to find an appropriate etch regime to make sure that all structures are released and to adjust the etch depth in the gratings of type 1 to 7.5 µm as close as possible, it was necessary to carry out etch tests with varying pre-etch depth. Furthermore, it was found to be critical to leave very thin membranes in large open areas (e.g. for the optical fibers) before photoresist removal (in oxygen plasma) due to high risk of cracking. Therefore, the pre-etch depth has been finally increased so that these large areas are already released after this step. Figure 9 shows several overview and detail SEM pictures of the obtained filter devices.

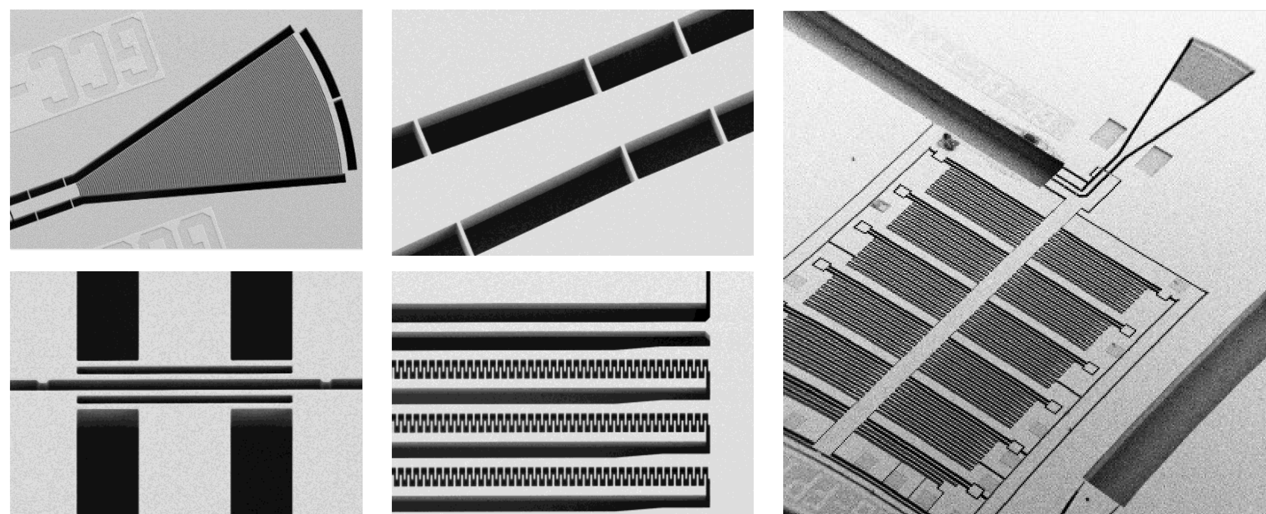

a) Details: Grating coupler type 1 (top left), Waveguide with taper (top right), Fabry-perot cavity with Bragg reflectors (bottom left), electrostatic comb drive electrodes and spring

b) Overview: tunable filter with waveguides and couplers

Figure 9. SEM pictures of fabricated devices

5. RESULTS AND DISCUSSION

5.1 Measurement setup

The transmittance of the tunable FPI was tested with a quantum cascade laser source (QCL) covering the spectrum from 9.0 µm to 9.4 µm (QF9159C2, Thorlabs) and a LN_2-MCT detector (Bruker Optics). Polycrystalline infrared fibers (PIR240/300 from art photonics) with a core diameter of 240 µm were used to couple to the grating couplers and edge couplers on the wafer. For contacting the actuator pads a multiprobe was used. The measurement setup on the wafer prober is shown in Figure 10a. Figure 10b shows the microscope view of the measurement setup on wafer prober. The tunable filter is coupled with fiber and grating coupler to the external QCL source, the output is coupled via edge coupling to the

Downloaded From: https://www.spiedigitallibrary.org/conference-proceedings-of-spie on 14 Nov 2023
Terms of Use: https://www.spiedigitallibrary.org/terms-of-use

MCT detector. The edge coupling is better suited for output coupling than for input coupling as the cross section of the fiber is bigger than the cross section of the waveguide. Compared to the state of the art [14] we use the grating coupler for a multi-mode waveguide. The higher thickness of waveguide and coupler compared to single-mode waveguides reduces the coupling efficiency significantly. For this reason, the measured detector signal was weak, but still the performance of the optical filter could be tested.

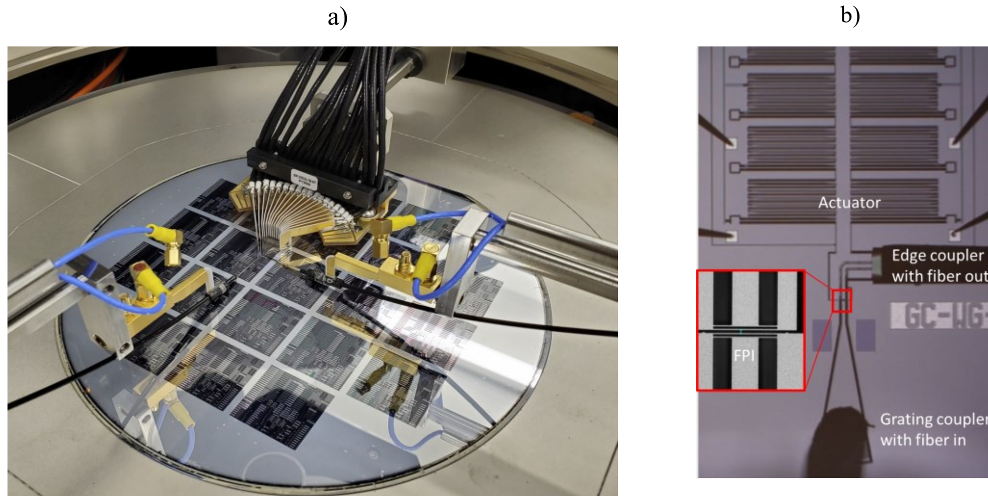

Figure 10. a) Measurement setup on wafer prober, with optical fibers and multi probe. b) Microscope view of measurement setup on wafer prober. The tunable filter is coupled with fiber and grating coupler to the external QCL source, the output is coupled via edge coupling to the MCT detector.

5.2 Tunable FPI

The parameters of two fabricated FPI samples have been investigated and compared to the design values.

The FPI reflector dimensions were measured with a SEM (see Figure 11). Table 1 shows the measured values compared to the design values for the thicknesses of the silicon and the air layers of the fixed and the movable reflector. The precision of the measurement is approximately ±50 nm. For this reason, the measured values are given in a resolution of 50 nm. Compared to the layout the silicon was over etched. The initial gap size (design value 3.2 µm) may be influenced by charge in the SEM and is not recorded here, but may be widened as well with a similar overetching.

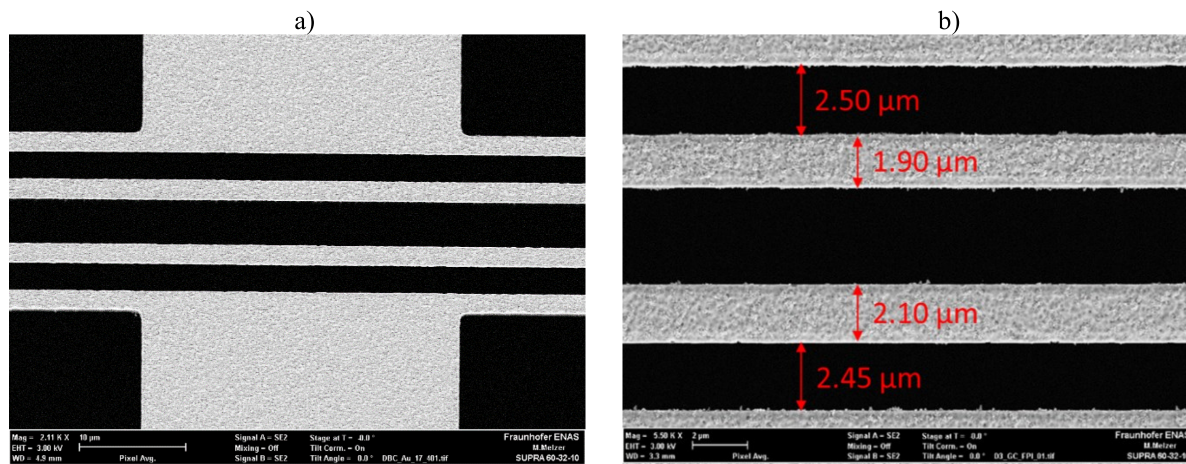

Figure 11. a) SEM picture of filter with distributed bragg reflectors b) measurement of reflector layer thicknesses of FPI 1

Downloaded From: https://www.spiedigitallibrary.org/conference-proceedings-of-spie on 14 Nov 2023
Terms of Use: https://www.spiedigitallibrary.org/terms-of-use

Table 1. Measured values of reflector layer thicknesses compared to design.

		Designed FPI	FPI sample 1	FPI sample 2
Silicon layer	Fixed reflector	2.06 µm	1.90 µm	1.90 µm
	Movable reflector	2.06 µm	2.10 µm	1.90 µm
Air layer	Fixed reflector	2.35 µm	2.50 µm	2.55 µm
	Movable reflector	2.35 µm	2.45 µm	2.50 µm

The over etching leads to a shift of the FPIs central wavelength. This is shown by simulations using the measured values. Compared to the results of the simulation with the values from design (Figure 3), the central wavelength of the FPI is now shifted to lower wavelengths (Figure 12). For reflector distance of 4.7 µm, for example, the central wavelength is 9.23 µm for the simulation with design values and 9.13 µm for simulation with the values measured with SEM. This is a wavelength shift of 100 nm.

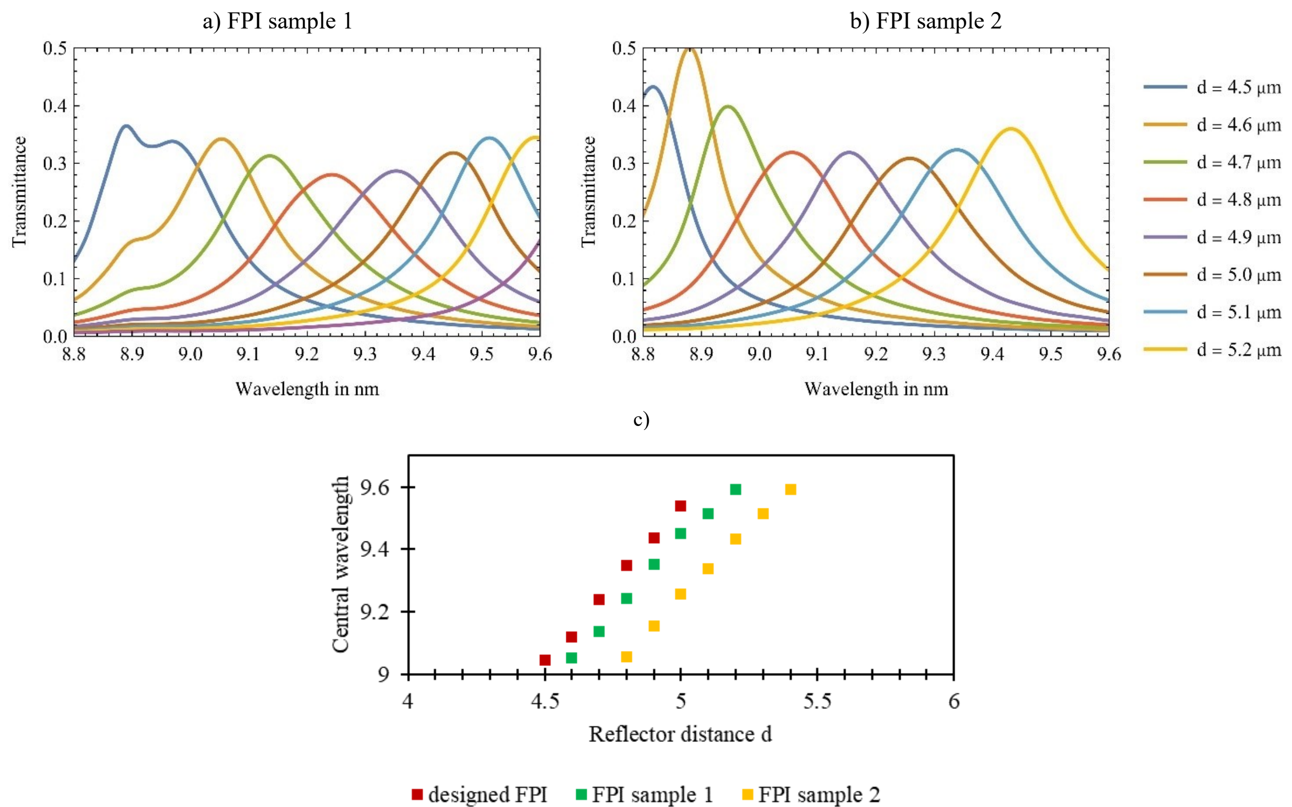

Figure 12. Transmittance for different resonator distances using measured values of layer thicknesses (simulated with CST Microwave Studio®) a) FPI sample 1, b) FPI sample 2. c) simulated tuning characteristic of the central wavelength comparing designed and measured values of layer thicknesses.

For a high filter transmittance, the verticality and the vertical alignment of both reflectors are very important. The vertical alignment was evaluated using a white light interferometer (Zygo). The measurement shows a slight distortion of the actuator in released state, resulting in a vertical displacement of the reflector at actuator side of -0.18 µm (Figure 13). This means that the effective area of the filter is reduced from 15 µm x 30 µm to 14.82 µm x 30 µm. For the design with multimode waveguides this displacement is not critical, as it is small compared to the whole reflector area. But it shows one more difficulty for a realization of in-plane FPI in single mode waveguides where the waveguide height needs to be very small (< 1.5 µm).

Downloaded From: https://www.spiedigitallibrary.org/conference-proceedings-of-spie on 14 Nov 2023
Terms of Use: https://www.spiedigitallibrary.org/terms-of-use

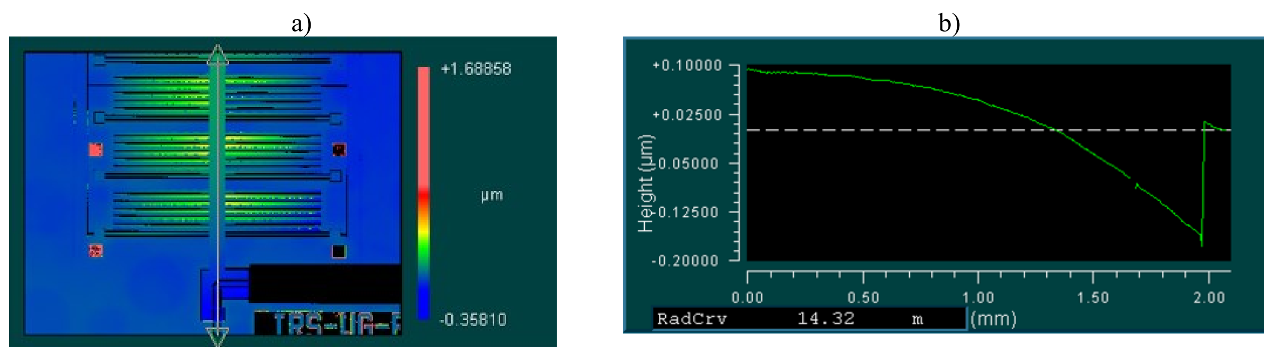

Figure 13. WLI measurement of actuator distortion a) surface map b) surface profile in direction of actuation (height difference between right and left reflector can be seen at profile position of approx. 2mm)

The analysis of the tuning characteristic of the actuator is very important for the application of the filter. As described above the actuator is driven with constant voltage and the tuning is achieved with 8bit digital actuator setpoints (0 to 255). The reflector distance allocated to each setpoint needs to be known for further characterization of the filter performance. To achieve this the change of the reflector distance was measured for the 6 most significant bits using a planar motion analyzer (MSA-600 from Polytec). Figure 14 shows the characteristic curve of two different actuator samples. Actuator sample 1 is controlled with 30 V actuation voltage, actuator sample 2 with 25 V actuation voltage. With the actuation voltage of 30 V, at setpoint 180 the travel limit set by stoppers is reached. For 25 V, the deflection per bit is lower; hence the full bit range can be used to reach the travel limit. The expected linear dependency of the deflection with regard to the digital setpoints is clearly visible for both actuation voltages. For further evaluations the total distance between both reflectors needs to be known. To calculate this value, the distance in released state was measured with an optical microscope. The distance in released state and the change of the reflector distance were added to get the reflector distance for every setpoint.

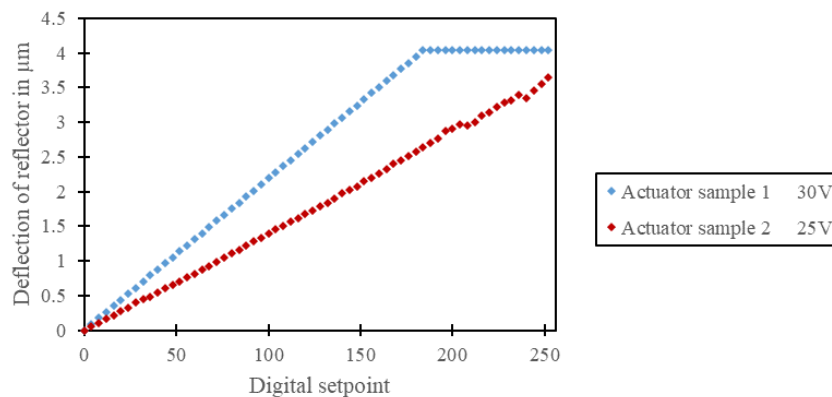

Figure 14. Reflector distance over digital actuator value, actuator sample 1 for 30 V actuation voltage, actuator sample 2 for 25 V

A quantum cascade laser (Thorlabs) with an emission in the range of 9…9.4 µm together with a MCT detector has been used for first evaluation of the tuning ability of the filter. For comparison, the laser spectrum was first measured with FTIR (see Figure 15).

Downloaded From: https://www.spiedigitallibrary.org/conference-proceedings-of-spie on 14 Nov 2023
Terms of Use: https://www.spiedigitallibrary.org/terms-of-use

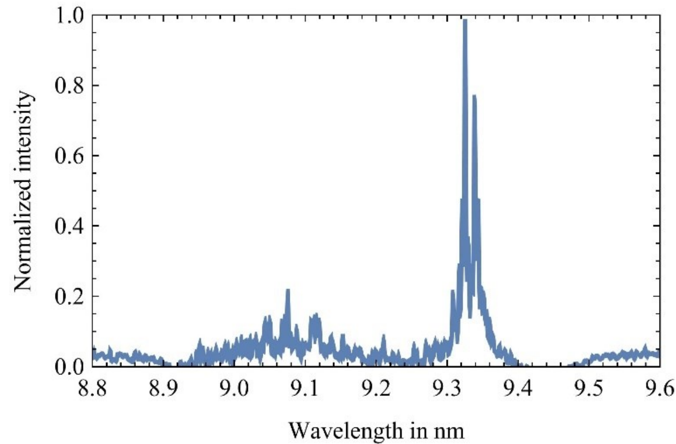

Figure 15. QCL spectrum measured with FTIR

When scanning with the filter over the emission wavelength range of the QCL, the transmitted spectrum is the result of the combination of both spectral characteristics and should be recorded on the detector. The measured laser spectrum together with the simulated FPI characteristics shown in Figure 12a and b were used to calculate an estimated transmittance as function of reflector distance (see Figure 16). It can be seen, that the over etched silicon layers, with lower thickness than designed cause a shift of the estimated transmittance to higher reflector distances.

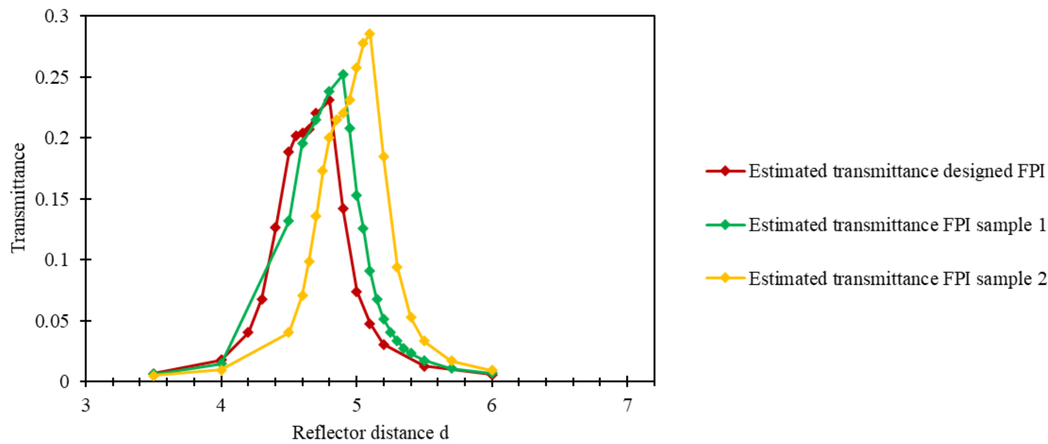

Figure 16. Estimated transmission, scanning with the FPI over the emission wavelength range of the QCL. With FPI as designed and based on measured geometry of the reflectors (FPI sample 1 and FPI sample 2).

The measured transmission characteristics with respect to the digital actuator values is presented in Figure 17. FPI sample 1 was actuated with 30 V and FPI sample 2 with 25 V. The functionality of the filter as wavelength selective element is clearly visible.

Downloaded From: https://www.spiedigitallibrary.org/conference-proceedings-of-spie on 14 Nov 2023
Terms of Use: https://www.spiedigitallibrary.org/terms-of-use

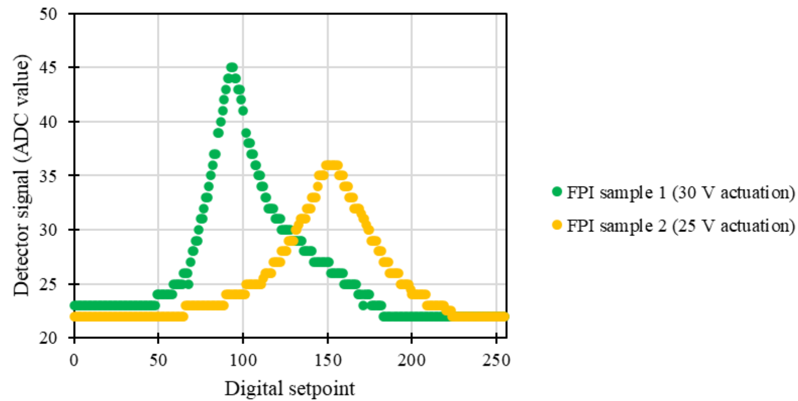

Figure 17. Measured transmittance of the quantum cascade laser measured with MCT detector and the two samples of tunable in-plane FPIs as wavelength selective element. Sample 1 was actuated with 30 V and sample 2 with 25 V.

In order to get the final transmission spectrum with respect to the reflector distance in the filter, several separate measurement data have to be combined and re-calculated, as our measurement setup does so far not allow to measure the reflector distance directly when actuating the filter together with the laser.

For comparison of simulated and measured data, the measured transmittance data from Figure 17 was transformed to a function of reflector distance. To achieve this the actuator characteristic curve from Figure 14 together with the distance in released state were used to transform the x-axis of the transmission measurement from digital setpoint values to reflector distance values. Now it is possible to compare these values with the simulated data from Figure 16.

For better understanding the data analysis workflow is shown in Figure 18.

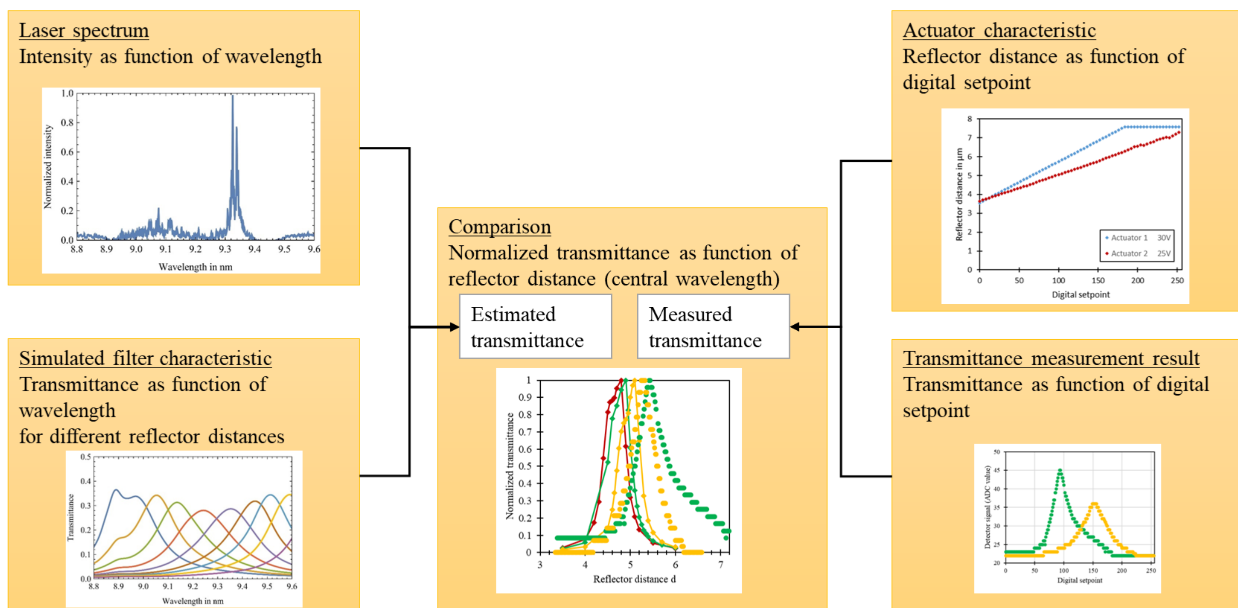

Figure 18. Workflow of measurement data analysis

Figure 19a shows the estimated and the measured transmittance curves as a function of the reflector distance. The estimated transmittance is taken from Figure 16. Here all curves are normalized with respect to the maximum transmittance. To get the transmittance as a function of wavelength the tuning characteristic from Figure 12c was used to evaluate the wavelength corresponding to each reflector distance. The result is shown in Figure 19b.

Downloaded From: https://www.spiedigitallibrary.org/conference-proceedings-of-spie on 14 Nov 2023
Terms of Use: https://www.spiedigitallibrary.org/terms-of-use

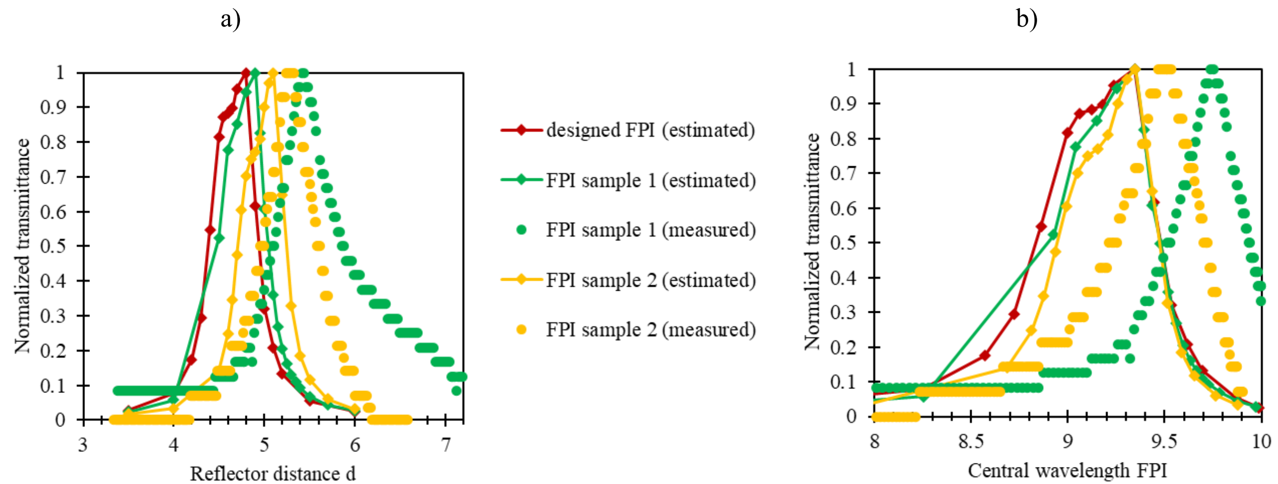

Figure 19. Comparison of estimated and measured transmittance of the quantum cascade laser measured with MCT detector and tunable in-plane FPI as wavelength selective element a) as a function of reflector distance, b) as a function of central wavelength. The curves are normalized with respect to the maximum transmittance.

The transmittance peaks based on the measurement of two individual devices show a shape similar to the estimated curves, however, the profile of the laser is less clearly visible. This might be caused by the low resolution of the detector signal, which is caused by a weak signal due to coupling losses.

The main difference compared to the estimated curves is the shift of the measured curved to a larger reflector distance (respectively larger wavelength). In Figure 19a it is visible that the simulated curves which take the measured layer thickness into account fit better to the measured results, however revealing still relatively large difference depending on the individual investigated dies. Especially for FPI sample 1 the difference is large. The authors assume that this difference is partly caused by inaccuracy in the measurement of the reflector distance and the layer thicknesses. The released actuator state was only measured with an optical microscope with a precision of approximately ±150 nm and the SEM measurement of the layer thicknesses has a precision of approximately ±50 nm. Furthermore, the actuator characteristic was taken from a separate measurement and the actuator is connected with probe needles, which may influence the initial reflector distance by applying local stress on the only 15 µm thick filter device. In addition, changes in the QCL spectrum were observed. Although the temperature and current of the laser were controlled, a deviation of the spectrum could still be observed after each new power-up.

An additional important point regarding deviations between calculation and measurement is the material characteristic. The refractive index and the extinction coefficient of the used silicon device layer are not exactly specified. The resistivity is specified > 1 kΩcm compared to 3 kΩcm taken for the simulation. Furthermore, the spectral characteristics of the grating coupler and the edge coupler can influence the result.

6. CONCLUSION

An in-plane tunable Fabry-Pérot Interferometer integrated in a multimode silicon waveguide for long infrared wavelengths was presented. Compared to other FPIs reported in literature the distributed Bragg reflectors have a small area of 15 µm by 30 µm perpendicular to the direction of light propagation. With this size the absorption of the reflector is simulated to be >6% resulting in a simulated peak transmittance of >25% and a FHWM of 270 nm.

The filter was fabricated using a modified cavity SOI technology based on an improved Si etch process with low sidewall roughness.

The FPI was coupled into the optical measurement setup using grating couplers and edge couplers. It was successfully tested with a 9.0 µm to 9.4 µm laser source (from Thorlabs) and a MCT detector (Bruker Optics). The filter characteristics was obtained with a digital electrostatic actuator operated with 30 V maximum voltage, hereby providing a maximum travel range of the filter of up to 4 µm (restricted by the design of the stoppers).

Downloaded From: https://www.spiedigitallibrary.org/conference-proceedings-of-spie on 14 Nov 2023
Terms of Use: https://www.spiedigitallibrary.org/terms-of-use

A drawback of the presently designed waveguide structures is the high absorption of silicon in the addressed wavelength range of 9.0 µm to 9.4 µm causing high propagation loss. For sufficient output intensity it is necessary to keep the waveguides short. However, the design can be adopted to different wavelength ranges by changing the reflector design.

It was found that the filter characteristics is sensitive to deviations of the real reflector geometries from the ideal ones. The overetching leads to smaller H layers and wider L layers. For further fabrication the over etching can be reduced by including a retaining dimension in the design.

Further work will focus on more detailed analysis of the whole measurement chain in order to find out the sources for differences between design and measurement data.

The presented FPI can be used as modulator or as wavelength selective element in chip integrated spectrometers.

7. ACKNOWLEDGEMENT

This research was partially funded by the Federal Ministry of Education and Research of Germany (BMBF) in the project PHiPMEMs (FKZ: 13N14928) and by the project 'ESAIRQ – Environmental Sensors for Air Quality' under the PENTA (16113) label endorsed by EUREKA Member Countries. The German part of the project is funded by the BMBF (FKZ: 16ES0827).

REFERENCES

[1] Chen, S, Zhang, Y., Hong, X. and Li, J.: *"Technologies and applications of silicon-based micro-optical electromechanical systems: A brief review,"* Journal of Semiconductors, vol. 43, Art. no. 8, (Aug. 2022).

[2] Ghoname, A. O., Sabry, Y. M., Anwar, M., and Khalil, D.: *"Attenuated total reflection (ATR) MEMS FTIR spectrometer,"* in MOEMS and Miniaturized Systems XIX, vol. 11293, pp. 170–175 (2020).

[3] Zhang, L., Chen, J., Ma, C., Li, W., Qi, Z. and Xue, N.: *"Research Progress on On-Chip Fourier Transform Spectrometer,"* Laser & Photonics Reviews, vol. 15, Art. no. 9 (2021).

[4] Wang, Z. and Zappe, H.: *"An Ultra-miniaturized Mid-infrared Spectrometer with no Moving Parts for Photochemical Analysis,"* in 2019 International Conference on Optical MEMS and Nanophotonics (OMN), pp. 132–133 (July 2019).

[5] Liu, W., Ma, Y., Chang, Y., Dong, B., Wei, J., Ren, Z. and Lee, C.: *"Suspended silicon waveguide platform with subwavelength grating metamaterial cladding for long-wave infrared sensing applications,"* Nanophotonics, vol. 10, no. 7, pp. 1861-1870 (2021).

[6] Sánchez-Postigo, A., Gonzalo, J., Wangüemert-Pérez, J., Soler Penadés, A., Ortega-Moñux, M., Nedeljkovic, R., Halir, F., El Mokhtari Mimun, Y., Xu Cheng, Z., Qu, A., Khokhar, Z., Osman, A., Cao, W.,. Littlejohns, C. G., Cheben, P., Mashanovich, G.Z, Molina-Fernández, Í.: *"Mid-infrared suspended waveguide platform and building blocks"*, IET Optoelectron., vol. 13 iss. 2, pp. 55-61 (2019).

[7] Tombez, L., Zhang, E.J., Orcutt, J.S., Kamlapurkar, S. and. Green, W. M. J.: *"Methane absorption spectroscopy on a silicon photonic chip,"* Optica, vol. 4, Art. no. 11 (Oct. 2017).

[8] Chandra, V., Ranjan, R.: *"Performance analysis of different slot waveguide structures for evanescent field based gas sensor applications",* Opt Quant Electron, vol. 53, pp. 457 (2021).

[9] Ranacher, C., Consani, C., Tortschanoff, A., Jannesari, R., Bergmeister, M., Grille, T., Jakoby, B.: *"Mid-infrared absorption gas sensing using a silicon strip waveguide"*, Sensors and Actuators A: Physical, vol. 277, pp. 117-123 (2018).

[10] Kita. D. et al.: *"Chip-scale high-performance digital Fourier Transform (dFT) spectrometers,"* in Next-Generation Spectroscopic Technologies XII (May 2019).

[11] Fathy, A. et al.: *"MEMS FTIR optical spectrometer enables detection of volatile organic compounds (VOCs) in part-per-billion (ppb) range for air quality monitoring,"* in MOEMS and Miniaturized Systems XVIII (Mar. 2019).

[12] Zhang, L., Chen, J., Ma, C., Li, W., Qi, Z. and Xue, N.: *"Research Progress on On-Chip Fourier Transform Spectrometer,"* Laser & Photonics Reviews, vol. 15, Art. no. 9 (2021).

[13] Sabry, Y. M., Eltagoury, Y. M., Shebl, A., Soliman, M., Sadek, M. and Khalil, D.: *"In-plane deeply-etched optical MEMS notch filter with high-speed tunability,"* Journal of Optics, vol. 17, Art. no. 12 (Oct. 2015).

Downloaded From: https://www.spiedigitallibrary.org/conference-proceedings-of-spie on 14 Nov 2023
Terms of Use: https://www.spiedigitallibrary.org/terms-of-use

[14] Sánchez-Postigo, A., Ortega-Moñux, A., Pereira-Martín, D., Molina-Fernández, Í., Halir, R., Cheben, P., Soler Penadés, J., Nedeljkovic, M., Mashanovich, G.Z. and Wangüemert-Pérez, J.G.: *"Design of a suspended germanium micro-antenna for efficient fiber-chip coupling in the long-wavelength mid-infrared range,"* Opt. Express 27, pp. 22302-22315 (2019).

[15] Steudel, A., *"Fortschritte in Leistungsfähigkeit und Anwendungsmöglichkeit des Fabry-Perot-Interferometers,"* Naturwissenschaften 44(8), 249–255 (1957).

[16] Atherton, P. D., Reay, N. K., Ring, J., Hicks, T. R.: *"Tunable Fabry-Perot filters,"* Opt. Eng 20(6), 806-814 (1981).

[17] Macleod, H.A.: *"Thin-Film optical filters"*, IoP, Bristol and Philadelphia, (2001).

[18] Lin, Y. and Lee, C.: *"Tunable fabry-perot filter using hybrid integrated grating and slot microstructures,"* Journal of Microelectromechanical Systems, vol. 23, pp. 1009–1011 (Oct 2014).

[19] Omran, H., Sabry, Y. M., Sadek, M., Hassan, K. and Khalil, D.: *"Wideband subwavelength deeply etched multilayer silicon mirrors for tunable optical filters and ss-oct applications,"* IEEE Journal of Selected Topics in Quantum Electronics, vol. 21, pp. 157–164 (July 2015).

[20] Goh, S.C.K., Chen, N., Shiau, L.L.,. Tay, B.K., Lee, C. and Tan, C. S.: *"Deposited poly-si as on-demand linewidth compensator for on-chip fabry–perot interferometer and vertical linear variable optical filter bandpass and passband manipulation,"* Journal of Micromechanics and Microengineering, vol. 29, p. 047001 (Feb 2019).

[21] Shkondin, E. et al.: *"Large-scale high aspect ratio Al-doped ZnO nanopillars arrays as anisotropic metamaterials,"* Optical Materials Express, vol. 7, Art. no. 5 (Apr. 2017).

[22] Wecker. J. et al.: *"Multi-Mode Silicon Waveguides at Long Infrared Wavelengths,"* 2022 Smart Systems Integration (SSI), pp. 1-6, doi: 10.1109/SSI56489.2022.9901435 (2022).

[23] Sarajlic, E., Collard, D., Toshiyoshi, H., Fujita, H.: *"12-bit microelectromechanical digital-to-analog converter of displacement: Design, fabrication and characterization",* 2007-01 IEEE 20th International Conference on Micro Electro Mechanical Systems (MEMS) p. 679-682 (2007).

[24] Pitchai, P., Uma, G., Mangalanathan, U.: *"Design and Simulation of MEMS-Based Digital-to-Analog Converters for In-Plane Actuation 2017-04 Arabian Journal for Science and Engineering"* , Vol. 42 p. 4991–5001(2017)

[25] Billep, D., Hiller, K., Küchler, M. Schröter, B., Dienel, M., Scheibner, D., Gessner, T: *"Bonding and deep RIE: a powerful combination for high-aspect-ratio sensors and actuators"*, Proc. of SPIE, Vol. 5715 pp. 80–91 (2005).

[26] Gao, F. et al: *"Smooth silicon sidewall etching for waveguide structures using a modified Bosch process"*, J. Micro/Nanolith. MEMS MOEMS 13(1), 013010 (2014)

Downloaded From: https://www.spiedigitallibrary.org/conference-proceedings-of-spie on 14 Nov 2023
Terms of Use: https://www.spiedigitallibrary.org/terms-of-use